

Cryoegg: development and field trials of a wireless subglacial probe for deep, fast-moving ice

Michael Prior-Jones¹, Elizabeth Bagshaw¹, Jonathan Lees², Lindsay Clare³, Stephen Burrow³, Mauro A Werder⁴, Nanna B. Karlsson⁵, Dorte Dahl-Jensen^{6,7}, Thomas R. Chudley⁸, Poul Christoffersen⁸, Jemma Wadham⁹, Samuel H Doyle¹⁰, Bryn Hubbard¹⁰

¹ School of Earth and Ocean Sciences, Cardiff University, Cardiff, UK (prior-jonesm@cardiff.ac.uk; bagshawe@cardiff.ac.uk)

² School of Engineering, Cardiff University, Cardiff, UK

³ Department of Aerospace Engineering, University of Bristol, Bristol, UK

⁴ Laboratory of Hydraulics, Hydrology and Glaciology, ETH Zürich, Zürich, Switzerland

⁵ Geological Survey of Denmark and Greenland, Copenhagen, Denmark

⁶ Niels Bohr Institute, University of Copenhagen, Copenhagen, Denmark

⁷ Center for Earth Observation Science, University of Manitoba, Winnipeg, Canada

⁸ Scott Polar Research Institute, University of Cambridge, Cambridge, UK

⁹ School of Geographical Sciences, University of Bristol, Bristol, UK

¹⁰ Department of Geography and Earth Sciences, Aberystwyth University, Aberystwyth, UK

This paper is a non-peer-reviewed preprint submitted to EarthArXiv. It has previously been submitted to Journal of Glaciology for peer-reviewed publication.

1 Cryoegg: development and field trials of a wireless subglacial probe for deep, fast-moving ice

2 Michael Prior-Jones¹, Elizabeth Bagshaw¹, Jonathan Lees², Lindsay Clare³, Stephen Burrow³, Mauro A
3 Werder⁴, Nanna B. Karlsson⁵, Dorthe Dahl-Jensen^{6,7}, Thomas R. Chudley⁸, Poul Christoffersen⁸, Jemma
4 Wadham⁹, Samuel H Doyle¹⁰, Bryn Hubbard¹⁰

5 ¹School of Earth and Ocean Sciences, Cardiff University, Cardiff, UK (prior-jonesm@cardiff.ac.uk;
6 bagshawe@cardiff.ac.uk)

7 ²School of Engineering, Cardiff University, Cardiff, UK

8 ³Department of Aerospace Engineering, University of Bristol, Bristol, UK

9 ⁴Laboratory of Hydraulics, Hydrology and Glaciology, ETH Zürich, Zürich, Switzerland

10 ⁵Geological Survey of Denmark and Greenland, Copenhagen, Denmark

11 ⁶Niels Bohr Institute, University of Copenhagen, Copenhagen, Denmark

12 ⁷Center for Earth Observation Science, University of Manitoba, Winnipeg, Canada

13 ⁸Scott Polar Research Institute, University of Cambridge, Cambridge, UK

14 ⁹School of Geographical Sciences, University of Bristol, Bristol, UK

15 ¹⁰Department of Geography and Earth Sciences, Aberystwyth University, Aberystwyth, UK

16 ABSTRACT

17 Subglacial hydrological systems require innovative technological solutions to access and observe.
18 Wireless sensor platforms can be used to collect and return data, but their performance in deep and
19 fast-moving ice requires quantification. We report experimental results from Cryoegg: a spherical
20 probe that can be deployed into a borehole or moulin and transit through the subglacial hydrological
21 system. The probe measures temperature, pressure and electrical conductivity in-situ and returns all
22 data wirelessly via a radio link. We demonstrate Cryoegg's utility in studying englacial channels and
23 moulins, including in-situ salt dilution gauging. Cryoegg uses very high frequency (VHF) radio to
24 transmit data to a surface receiving array through up to 1.3 km of cold ice - a significant improvement
25 on the previous design. The wireless transmission uses Wireless M-Bus on 169 MHz; we present a
26 simple radio link budget model for its performance in cold ice and experimentally confirm its validity.
27 Cryoegg has also been tested successfully in temperate ice. The battery capacity allows measurements
28 to be made every two hours for more than a year. Future iterations of the radio system will enable
29 Cryoegg to transmit data through up to 2.5 km of ice.

30 INTRODUCTION

31 The presence and behaviour of water in the subglacial environment governs the response of ice to
32 climate warming. Meltwater generated on the surface makes its way to the bed via networks of
33 moulins, cracks and crevasses (Chu, 2014; Flowers, 2018). Once at the bed, it flows to the ice margins
34 either through a subglacial drainage network consisting of inefficient linked cavities (Iken and
35 Bindschadler, 1986; Walder, 1986; Kamb, 1987), efficient channels carved into rock, ice or the
36 sediment below (Röthlisberger, 1972; Nye, 1976; Clarke, 1987; Ng, 2000), or a combination of both
37 (Hoffman and others, 2016). The configuration of the drainage network determines the subglacial
38 water pressure and how much of the ice-bed interface is in contact with liquid water. Contact
39 promotes sliding (Kamb, 1970; Iken, 1981; Schoof, 2010), which in turn can cause ice to accelerate
40 downstream. In recent years, the relationship between meltwater supply and ice acceleration has
41 been reevaluated in light of observations from the margins of the Greenland Ice Sheet that
42 demonstrate a seasonal evolution of subglacial drainage systems (Chandler and others, 2013;
43 Tedstone and others, 2015) commonly observed in Alpine systems (Nienow and others, 2005). Early
44 in the melt season, an increased flux of meltwater is routed to the bed and the low capacity,
45 inefficiently linked cavity system is forced to expand, forming efficient channels that can transport
46 substantial volumes of water. This reduces the area of the bed in contact with water, and potentially,

47 regulates the flow of ice (Sole and others, 2011; Tedstone and others, 2015; Nienow and others, 2017;
48 Flowers, 2018). The defining feature of these different drainage configurations is the water pressure:
49 channelised systems operate at lower pressure than linked cavities, thus measurement of the
50 subglacial water pressure can be used to determine the likely structure of the drainage system, and
51 hence the acceleration response of the ice to increased surface melt inputs.

52 In addition to water pressure, other parameters may provide clues as to the structure of the drainage
53 system, but distinction between drainage system types is challenging. Temperature can be used to
54 assess whether the bed is at the pressure melting point, and the residence time of water in the system
55 can be used, in conjunction with pressure, to assess how efficiently the meltwater transits the system.
56 Long residence times are common in linked cavity systems, which results in prolonged contact
57 between meltwater and subglacial sediment (Tranter and others, 2002). This promotes chemical
58 weathering and changes the composition of the meltwater, so meltwater chemistry is a good indicator
59 of drainage system structure. Chemical composition is challenging to assess in situ, but a
60 measurement of the total dissolved solids can be easily obtained via a measurement of electrical
61 conductivity (Hubbard and others, 1995).

62 These three parameters (pressure (P), temperature (T) and electrical conductivity (EC)) are relatively
63 easy to measure via electronic sensors and can thus be combined to provide information on subglacial
64 drainage that could not be detected from the surface. Measuring these parameters subglacially is,
65 however, extremely challenging, particularly beneath thick, fast flowing ice. Yet it is these fast-flowing
66 sectors that govern the response of large ice masses to climate warming, since they transfer significant
67 volumes of ice to the ocean (Pritchard and others, 2009; Broeke and others, 2016). Drilling boreholes
68 through a glacier to access subglacial hydrological channels is logistically demanding and disturbs the
69 system that is under study. Once boreholes are drilled, implanting cabled sensors is possible, but ice
70 motion causes cables to flex and eventually break (Iken and others, 1993; Doyle and others, 2018). In
71 fast-flowing ice, data capture is thus limited to days or weeks. An alternative method is therefore
72 required that can capture these relatively simple electrical measurements and return them to the
73 surface without requiring a physical connection. A wireless radio frequency (RF) system is ideal and
74 there is a long history of the use of RF propagation through ice (see Plewes and Hubbard, 2016 for a
75 review).

76 Here, we present trials of Cryoegg, a wireless sensor platform for use in deep ice. The use of a radio
77 link for subglacial telemetry has been proven by the work of the Glacsweb programme (Martinez and
78 others, 2004; Hart and others, 2019) and the WiSe project (Smeets and others, 2012). Previous work
79 (Bagshaw and others, 2014) showed that a 'Cryoegg' concept was feasible, namely a spherical sensor
80 platform containing all sensor, radio and datalogger components that could fit in a standard borehole
81 and travel through subglacial meltwater pathways: the electronics could be made sufficiently
82 compact, and that the radio link worked through up to 500m of ice. However, the radio link design
83 chosen proved unsuitable for performance in very deep ice, so design improvements were required.
84 In this paper we describe the redesign of Cryoegg to give enhanced radio link performance and show
85 the outcomes of field trials at sites in Greenland and the Swiss Alps.

86 In order to measure subglacial hydrological properties in deep polar ice, the enhanced Cryoegg had to
87 meet or exceed the following engineering constraints:

- 88 • An outer diameter of 120 mm or less, to fit into a standard ice core borehole
- 89 • A radio link capable of reaching the surface through 2,500 m of ice, the mean bed depth in
90 central Greenland (Morlighem and others, 2017)
- 91 • Survive and measure water pressure of up to 250 bar (equivalent to a water column of 2,500
92 m)
- 93 • Measure temperature, typically in the range from -30 to 0 °C
- 94 • Measure EC, typically in the range from 2 $\mu\text{S cm}^{-1}$ to 250 $\mu\text{S cm}^{-1}$
- 95 • A battery life capable of sustaining one measurement every 12 hours for a period of one year

96 RADIO LINK DESIGN

97 The success of the instrument depends principally on the performance of the radio link. The 2012
98 design (Bagshaw and others, 2014) used a simple frequency shift keying (FSK) transmitter operating
99 on 151 MHz and demonstrated a maximum range of 500 m in wet ice. To achieve a greater range, we
100 investigated alternative frequencies and transmission schemes. The power of a radio wave
101 propagating in “free space” (e.g. in air or vacuum) reduces according to an inverse square law with
102 distance - known as “geometric attenuation”. When the propagating wave reaches a receiving
103 antenna, the ability of that antenna to extract power from the incoming wave is the “effective
104 aperture”, and this depends upon the wavelength of the incoming wave. Antenna performance is
105 more usually characterised using the antenna gain, which is the ratio of the antenna’s effective
106 aperture in the direction of the main beam to the effective aperture of an “ideal” isotropic antenna
107 that receives signals equally well in all directions. Antennas are reciprocal devices and so their
108 characteristics (including gain) apply equally to both transmission and reception.

109 These effects are collectively described by the free space path loss equation, sometimes known as the
110 Friis transmission equation, which describes how a radio link performs in free space. The equation
111 assumes that the antennas are optimally pointed at one another and that their polarisations match,
112 otherwise there are further losses associated with pointing error and polarisation mismatch. The
113 original paper (Friis, 1946) presents the equation in terms of effective aperture, and in linear units.
114 The more commonly used version quoted here is expressed in terms of antenna gain and uses decibel
115 units.

116 Equation 1, adapted from Griffiths (1987, p. 12), is the free space path loss equation in decibel units:

$$117 P_{rx} = P_{tx} + G_{tx} + G_{rx} - 20 \log_{10} \left(\frac{4\pi d}{\lambda} \right) \quad (1)$$

- 118 • P_{rx} is power at the receiver, in dBW (dB relative to 1 watt)
- 119 • P_{tx} is power transmitted by the transmitter, in dBW
- 120 • G_{tx} is the gain of the transmitting antenna, in dBi (dB relative to the performance of an
121 isotropic antenna)
- 122 • G_{rx} is the gain of the receiving antenna, in dBi
- 123 • d is the distance between the transmitting and receiving antennas in metres
- 124 • λ is the wavelength of the transmission.

125 The last term of Equation 1 is known as the “free space path loss” (FSPL) and combines the geometric
126 attenuation due to distance with the apparent wavelength-related attenuation caused by the effective
127 aperture of the antennas. Consequently, the free space path loss equation gives us the rule of thumb

128 that lower frequencies (= longer wavelengths) appear to propagate further than higher frequencies..
 129 FSPL over 2500 m ranges from 70 dB at 30 MHz to 99 dB at 868 MHz (Table 1), depending on frequency.
 130

System	WiSe (Smeets)	eTracer, Cryoegg (2012), Glacswab (2013 – present)	Glacswab (2004 –2012)	LoRaWAN	Cryoegg (2019)
Frequency (MHz)	30	150	433	868	169
Distance (m)					
100	42.0	56.0	65.2	71.2	57.0
500	56.0	70.0	79.2	85.2	71.0
1000	62.0	76.0	85.2	91.2	77.0
1500	65.5	79.5	88.7	94.7	80.5
2000	68.0	82.0	91.2	97.2	83.0
2500	70.0	83.9	93.1	99.2	85.0

131 Table 1: Values of free space path loss in dB for several frequencies used by previous subglacial
 132 wireless transmission systems (Smeets and others, 2012; Bagshaw and others, 2014; Martinez and
 133 others, 2004; Hart and others, 2019), the industrial standard LoRaWAN (Low power Radio Wireless
 134 Area Network (About LoRaWAN® | LoRa Alliance®)) and the redesign of Cryoegg (see results section).
 135

136 FSPL applies to all radio links regardless of the propagating medium. However, where the medium is
 137 lossy the signal is further attenuated by the interaction between the wave and the medium. Ice is one
 138 such lossy medium. Whilst simple models can predict RF attenuation in pure ice, in reality, glacier ice
 139 is heterogeneous, varying in temperature, pore water and impurity content and it contains cracks,
 140 water pockets and debris. Ultra-high frequencies (UHF, 300 MHz–3 GHz) have been effective for
 141 transmission through deep, cold and uniform ice (Lewis and others, 2015), but any presence of water
 142 in this matrix quickly reduces success due to scattering and attenuative losses. The high frequency
 143 (HF, 3-30 MHz) and very high frequency (VHF, 30-300 MHz) bands have good penetration through ice,
 144 with wavelengths longer than typical englacial water bodies encountered along the transmission path
 145 (Smeets and others, 2012).

146 The attenuation of electromagnetic waves in glacial ice is reported in the study of high-energy
 147 neutrinos (Barwick and others, 2005; Barrella and others, 2011). Particle physicists and radio
 148 astronomers describe attenuation using *attenuation length* (L_α) in metres as a unit rather than the
 149 *attenuation coefficient* (α) in decibels per metre. The two are related by Equation 2 (Barrella and
 150 others, 2011):

$$151 \quad L_\alpha = \frac{1}{\ln \sqrt{10^{\frac{\alpha}{10}}}} \quad (2)$$

152 We can rearrange and simplify Equation 2 to allow us to convert attenuation length to attenuation
 153 coefficient in dB m⁻¹ (Equation 3). Some typical values of attenuation length are shown converted to
 154 dB per kilometre in Table 2.

$$155 \quad \alpha = \frac{20}{(\ln 10)L_\alpha} \quad (3)$$

156

Attenuation length (L_α), metres	Attenuation coefficient (α), dB km ⁻¹
100	86.9
200	43.4
300	29.0
400	21.7
500	17.4
600	14.5
700	12.4
800	10.9
900	9.7
1000	8.7
1500	5.8
2000	4.3
5000	1.7

158 Table 2: Attenuation length and corresponding attenuation coefficient from 100 to 5000 m

159 Attenuation lengths determined experimentally vary slightly by frequency (Barwick and others, 2005),
 160 with lower frequencies generally having longer attenuation lengths (and hence lower attenuation
 161 coefficients). Mitigating against both free-space and ice-related losses therefore points towards the
 162 use of lower frequencies for radio links within ice. However, low frequencies imply long wavelengths,
 163 which in turn requires physically large antennas, as an efficient antenna needs to be at least $\frac{1}{4}$ of a
 164 wavelength long. The WiSe system at 30 MHz has a wavelength of 10 metres and used half-wavelength
 165 dipole receiving antennas which were five metres long (Smeets and others, 2012). Large antennas
 166 become impractical to work with in the field, and we had the additional challenge of needing to fit our
 167 transmitting antenna into the 120 mm diameter Cryoegg enclosure. Our previous work used 151 MHz
 168 (wavelength 2 m), which had given satisfactory performance and allowed the receiving antenna to be
 169 easily carried in the field. The very small size of the Cryoegg enclosure meant that there was limited
 170 value in going to higher frequencies as the benefits of having a better-matched transmitting antenna
 171 were far outweighed by the additional free-space and ice-related losses. We therefore looked for a
 172 system that could operate in the VHF band (30-300 MHz).

173 For frequencies in the VHF range (30-300 MHz) the attenuation lengths reported (Barwick and others,
 174 2005; Barrella and others, 2011) range from 200 m to 3000 m. We take the worst-case figure of 200
 175 m (43.4 dB km⁻¹) as our design criterion for working in warm, wet ice and 400 m (21.7dB km⁻¹) as a
 176 conservative estimate for cold, dry ice (Table 2).

178 METHODS

179 Choice of transmission scheme

180 The term “transmission scheme” encompasses all the technical aspects of the radio link – the
181 modulation, error corrective coding, packetisation, and higher-level protocols. We required a
182 commercially available system designed for long battery life and for sending small amounts of data
183 over long distances, often sold as “internet of things” (IoT) systems. In particular, a number of low
184 power wide area network (LPWAN) technologies have been developed which aim to provide long-
185 range radio links to battery powered devices. The system we selected is Wireless M-Bus mode N1
186 (European Committee for Standardisation, 2013), which is intended for use in utility metering. It is
187 designed to offer very long battery life and sends data at 2.4 kbit s^{-1} . It incorporates error corrective
188 coding, which ensures that data received over the link does not contain errors introduced in transit,
189 and has optional cryptographic protection for security.

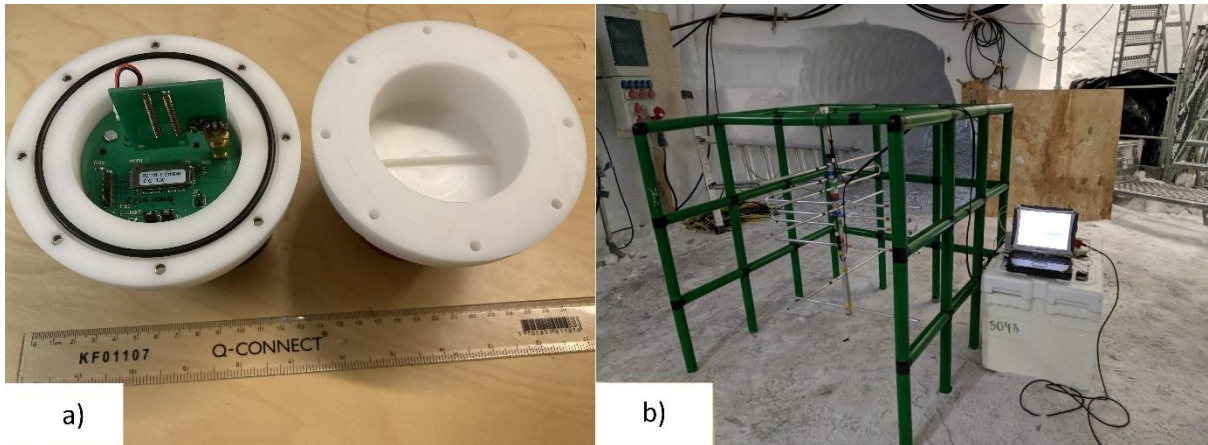
190 The appeal of this standard is that it operates in the 169 MHz frequency band, a relatively low
191 frequency compared with most of the other systems on the market. In Europe this 169 MHz frequency
192 band has been opened up for general license-free use (CEPT ECC Recommendation 70-03). Wireless
193 M-Bus is an open standard and a number of manufacturers provide implementations of it. This gives
194 confidence that the technology will remain available, whereas with a proprietary system carries a risk
195 of the product being discontinued.

196 The Radiocrafts RC1701HP-MBUS4 modem used is readily available (Digi-Key part number 1783-1048-
197 1-ND) and offers 0.5 W (27 dBm) power output on the 169 MHz band. One module is fitted to the
198 custom printed circuit board inside Cryoegg, configured as a transmitter. For the receiver, we use
199 Radiocrafts RC1701HP-MBUS4 demo kit (Digi-Key part number 1783-1004-ND) with one board
200 configured as a receiver. This board can be connected to a PC via USB and will output the decoded
201 data received over the radio link. A Python script running on the PC applies a timestamp to the
202 received packet data and records it in a log file. This approach avoids the need to have a source of
203 accurate time on board Cryoegg.

204 Antenna selection

205 The transmitting antenna inside Cryoegg is constrained by the physical size of the spherical case. We
206 sought a small antenna that had previously been proven to work on the 169 MHz band. We selected
207 the HA.10 from Taoglas, which consists of a pair of air-cored helical elements and a matching network.
208 To minimise use of conductive materials around the antenna, the upper hemisphere is devoted to the
209 antenna and the remaining electronics fit into the lower hemisphere (Figure 1a). The antenna is
210 matched to the modem module using a pair of small inductors.

211



212

213 Figure 1 – a) Cryoegg with upper casework removed b) receiving antenna mounted on plastic frame

214 The receiving antenna on the surface provides additional gain to the system to help overcome the
215 attenuation through the ice, and to compensate for the small size of the transmitting antenna – an
216 ideal antenna would be 450 mm long and Cryoegg’s diameter is only 120 mm. We elected to use a
217 pair of crossed Yagi-Uda antennas (Innovantennas), which provide a gain of around 8 dB individually.
218 They are combined through a 90° hybrid combiner (Mini-Circuits part number ZMSCQ-2-180BR+)
219 which makes them behave as a single circularly polarised antenna, but at the expense of 3dB loss in
220 the combiner. By transmitting with linear polarisation and receiving with circular polarisation, we
221 make the radio link performance relatively independent of Cryoegg’s orientation. This technique was
222 also used by the WiSe project team (Smeets and others, 2012).

223 The receiving antenna is about one metre long. In order to minimise disturbance to the antenna
224 pattern caused by metal parts close to the antenna elements, we used a modular plastic frame
225 (Quadro, Hamburg) to support the antenna, as shown in Figure 1b.

226 The radiation pattern of Cryoegg was assessed in a screened RF test chamber (at the Wolfson Centre
227 for Magnetics in Cardiff) lined with absorbent ferrite material to prevent multipath. A log-periodic
228 antenna was used to receive the signal and the signal level was observed using a spectrum analyser in
229 peak hold mode.

230 Link budget

231 A link budget is used to evaluate whether an attenuation-limited radio link will work in practice.
232 Starting with the power output of the transmitter, gains and losses in the system are totalled up and
233 compared to the sensitivity of the receiver. If the received power level is greater than the sensitivity,
234 the system will work. To allow some margin for unexpected attenuation, we aim for a received power
235 level several dB higher than the sensitivity. Link budgets are traditionally calculated in decibel units as
236 this allows the gains and losses to be added and subtracted (rather than multiplied and divided). Hence
237 we use decibel units of power, such as dBW: decibels relative to one watt, (0 dBW = 1W) or dBm:
238 decibels relative to one milliwatt (0 dBm = 1mW = -30 dBW, and +30 dBm = 1 W = 0 dBW).

239 The link budget calculation (Table 3) assumes a 2000 m borehole through cold ice, with the
240 attenuation coefficient estimated at 21 dB km⁻¹. The performance of the transmit antenna was
241 relatively poor, and so we estimated its gain at -15 dBi (dB relative to an isotropic antenna) based on
242 data from the manufacturer. For the 2000 m example shown here, the received signal margin is 10.5
243 dB.

			Link budget contribution	Units
Transmitter power	0.5	W	27.0	dBm
Coupling loss			-0.5	dB
Transmit antenna gain			-15.0	dBi
Distance to receiver	2	km		
Frequency	169	MHz		
FSPL			-83.0	dB
Attenuation coefficient for cold ice	21	dB/km		
Ice related loss			-42.0	dB
Crosspolarisation loss			-3.0	dB
Receive antenna gain			8.0	dBi
Total power at receiver			-108.5	dBm
Receiver sensitivity	-119	dBm		
Margin			10.5	dB

244 Table 3: Link budget calculation for Cryoegg in 2000 m borehole in cold ice (gains are positive values,
245 losses are negative).

246 Sensors

247 The Keller PA-20D pressure sensor, with 250 bar maximum, has a vacuum-sealed membrane and
248 communicates with the microcontroller via the widely-used digital I²C interface (Inter-Integrated
249 Circuit; (UM10204 I2C-bus specification and user manual, 2014)). It provides internal temperature
250 compensation, and supplies a temperature reading alongside the pressure reading, although the
251 manufacturer does not guarantee its performance at temperatures below 0 °C. Hence we provided
252 our own independent temperature sensor, details of which are below. The sensor provides a 16-bit
253 pressure reading to the microcontroller but uses only half the available range (the rest being used to
254 allow it to report pressures slightly beyond the calibrated range). This means that the smallest
255 pressure step reportable is 7.6 millibars. The nominal total error band is 1% of full scale, i.e. 2.5 bar,
256 but in practice we found we could reliably record changes in water pressure down to 0.1 bar (1m
257 hydrostatic pressure) during field experiments.

258 The temperature and EC sensors are adapted from earlier designs (Bagshaw and others, 2012, 2014).
259 The EC sensor consists of a square wave oscillator which supplies a 500 kHz waveform to a potential
260 divider consisting of a precision resistor and a pair of sense electrodes. The sense electrodes are a pair
261 of M3 stainless steel hex-headed bolts that protrude through the case. The AC waveform from the
262 midpoint of the potential divider passes through a precision rectifier and RC filter to produce a DC
263 voltage that varies inversely with EC between the sense electrodes. This is sampled by the
264 microcontroller's analogue-to-digital converter (ADC) and the resulting digital value is reported over
265 the radio link. The temperature sensor is a Pt1000 platinum resistance device, used in a full-bridge
266 configuration with three fixed resistors. It is driven by a current source and measured using an
267 instrumentation amplifier, with the output fed to the microcontroller's ADC. Cryoegg reports the
268 digital value from the ADC over the radio link, allowing calibration to be carried out externally. The
269 Pt1000 resistor is mounted to the back of one of the EC sense electrodes with a thermal pad, ensuring
270 that has thermal but not electrical contact.

271 Microcontroller selection

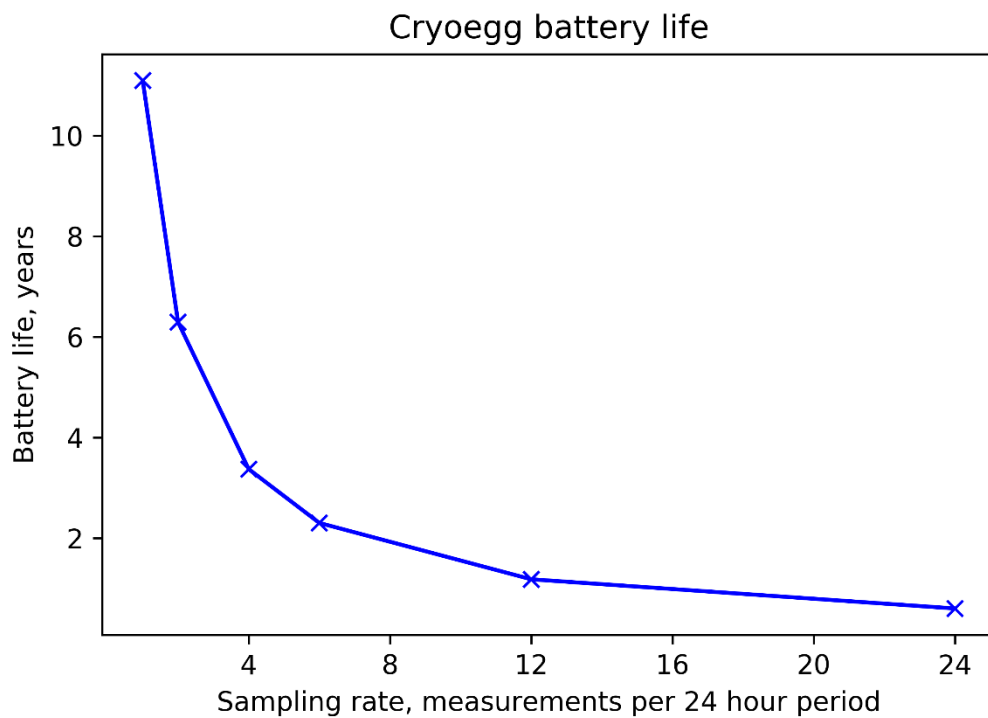
272 To maximise battery life, system power consumption should be as low as possible between
273 measurements. Cryoegg therefore has a “sleep” mode where all systems were powered down apart
274 from a system timer that wakes the main processor back up in time for the next measurement. The
275 STM32L433RCT6P microcontroller (STMicroelectronics) has a built-in timer (known as the Real Time
276 Clock module, RTC) which uses an external quartz crystal oscillator to provide reliable timekeeping at
277 very low power. The RTC draws around 500 nA at 3.3 V with the rest of the microcontroller shut down.
278 The microcontroller has a 32-bit ARM Cortex M4 processor that can be clocked at up to 80 MHz, 256
279 kB of flash memory and 64 kB of RAM. It has a wide range of internal peripherals, of which we use the
280 ADC for the temperature and EC sensors; I²C interface for the pressure sensor; and Universal
281 Asynchronous Receiver/Transmitter (UART) for communicating with the radio module. The
282 microcontroller also controls several power switches that enable and disable power to other parts of
283 the circuit.

284 Power supply design and power consumption

285 The radio modem module has relatively high power consumption during transmit – requiring 500 mA
286 at 3.3 V for less than 500 ms during each transmission, which puts a lot of demand on the battery and
287 power supply to be able to supply this peak current. A lithium-polymer rechargeable pouch cell can
288 supply sufficient peak current and be recharged between tests. The battery selected has a 3.7 V
289 nominal voltage and a capacity of 400 mAh.

290 Power from the battery is supplied unregulated to the microcontroller, and (via a MOSFET switch) to
291 the radio module. Using the unregulated supply means that no power is wasted by a regulator in
292 standby mode. However, we found that a regulated supply was necessary for the sensors, since
293 variations in battery voltage could affect their performance. A regulator IC with an enable input (ON
294 Semiconductor NCP115ASN330T2G) supplies 3.3 V to the sensors when enabled, and also provides
295 the ADC reference voltage to the microcontroller.

296 To estimate the battery life, we measured the power consumption of Cryoegg during transmission and
297 during sleep mode in the lab, using a logging multimeter (Mooshim Engineering Mooshimeter) that
298 could measure voltage and current from the battery simultaneously. The measure-and-transmit cycle
299 takes 3.2 seconds and consumes 0.5 J. The sleep mode current consumption proved to be too low for
300 the meter to measure (the lowest current it can record is 5 μ A). We therefore assume that the sleep
301 mode current consumption is that of the microcontroller only (since everything else is disabled) and
302 take the value quoted in the microcontroller datasheet of 500 nA.



303

304 Figure 2 - Cryoegg battery life with varying sampling rate

305

306 Figure 2 shows the results of the battery life calculations. The projected battery life is over 6 years at
 307 two measurements per day. Even allowing for some self-discharge in the battery, this gives scope to
 308 increase the measurement frequency. A measurement every 2 hours (i.e. 12 times per day) gives a
 309 battery life of just over a year. Table S1 in the Supplementary Information shows an example battery
 310 life calculation in more detail.

311 Mechanical design

312 We aimed to provide a simple and robust mechanical design that was straightforward to assemble for
 313 testing. The spherical casework is machined in two halves from acetal copolymer, a hard engineering
 314 plastic. The internal void is cylindrical, as shown in Figure 1a. The lower hemisphere has a flat side
 315 through which the sensors are mounted. The sensor PCB sits directly onto the bottom of the internal
 316 void and is secured in place by two M3 threaded spacers. We used Raytech Liquid Rubber potting to
 317 enclose the sensor PCB to help prevent leaks. There are two further PCBs that mount above the sensor
 318 PCB, which interconnect using multiway connectors. The processor PCB contains the microcontroller
 319 and associated components, and also provides mechanical support for the battery. The radio PCB is
 320 uppermost and supports the radio module, antenna connector, battery connector and headers for
 321 programming and debugging. The battery, a pouch cell, is sandwiched in the gap between the radio
 322 and processor PCBs. The antenna PCB connects to the radio PCB via an SMA connector and is
 323 supported by a groove in the crown of the upper hemisphere. This design allows the upper hemisphere
 324 to be easily removed for access to the electronics, and to connect the battery before deployment. The
 325 upper and lower hemisphere seal with a rubber O-ring and are held in place by eight machine screws.

326

327 **Software**

328 The software on the Cryoegg microcontroller is written in C, using the STM32 Hardware Abstraction
329 Libraries. The software goes through the following steps:

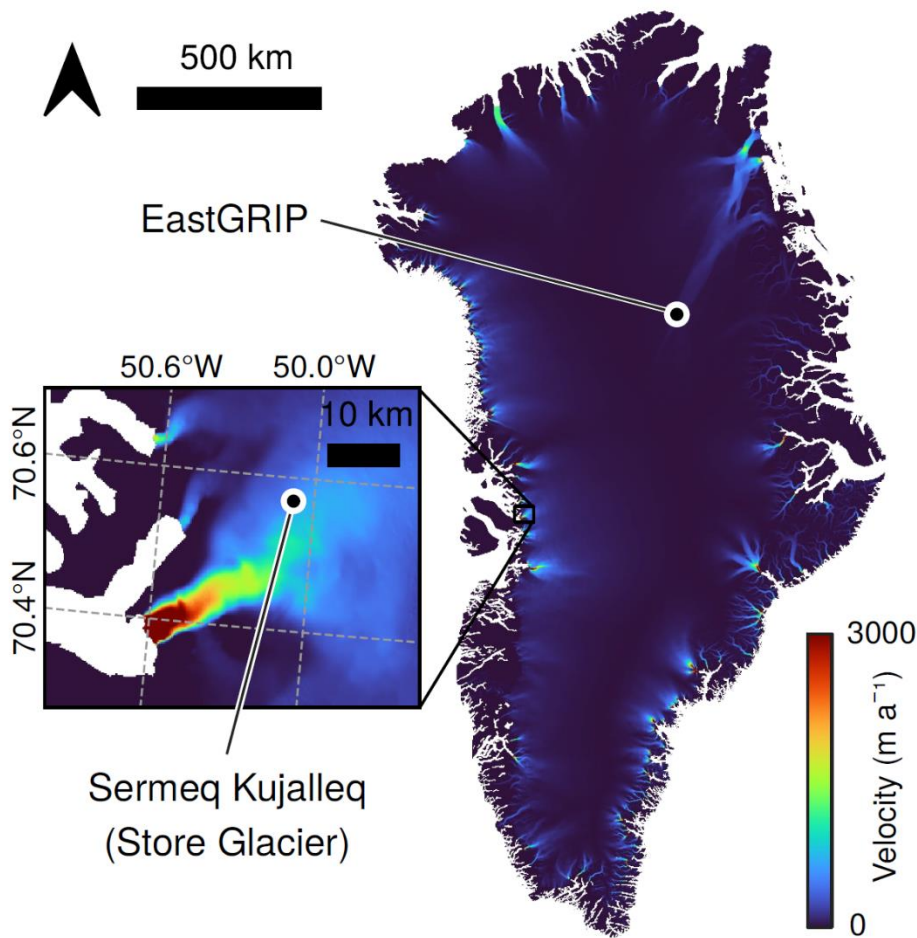
- 330 • Power up the sensors
- 331 • Make measurements
- 332 • Power down the sensors
- 333 • Power up the radio module
- 334 • Pack the sensor data into a data packet
- 335 • Send the data packet to the radio module to be transmitted
- 336 • Power down the radio module
- 337 • Set the sleep timer for the next measurement
- 338 • Enter deep sleep (“SHUTDOWN”) mode

339 On awakening from SHUTDOWN mode, the program restarts from the beginning, thus giving an
340 endless loop. The measurements are transmitted immediately after being made, and no data is stored
341 on Cryoegg, since we do not expect to retrieve Cryoegg after deployment. This does also mean that
342 any data transmitted by Cryoegg that is not received on the surface is lost.

343

344 **Field testing**

345 We conducted three field tests during July and August 2019 at two sites in Greenland (EastGRIP drill
346 site and Sermeq Kujalleq/Store Glacier) and one in Switzerland (Rhône Glacier).



347 Figure 3 - Velocity map of Greenland ice sheet flow, showing locations of EastGRIP and Sermeq
348 Kujalleq test sites in fast flowing ice. Data from MEaSUREs dataset of annual Greenland velocity for
349 2018 (Joughin and others, 2010; Joughin, 2017).

350 *East Greenland Ice Core Project site (EastGRIP)*

351 EastGRIP is located at N75° 38.05' W036° 00.22' on the North East Greenland Ice Stream (NEGIS), the
352 largest ice stream in Greenland, which drains 340,000 km² of the ice sheet and extends for over 1000
353 km inland (Figure 3). Approximately 150 km from the onset, it reaches speeds of 65 m a⁻¹ (Joughin and
354 others, 2010; Karlsson and Dahl-Jensen, 2015). The NEGIS is the location of the East Greenland Ice
355 core Project (EastGRIP), a unique project drilling an ice core into 2.5 km of fast flowing ice to
356 investigate ice stream beds (www.eastgrip.org). In summer 2019, the core had been drilled to 2 km
357 depth, leaving behind a 2 km borehole filled almost completely with drill fluid. The purpose of our
358 field trial at this site was to obtain a range test for the radio link and a pressure test for the mechanical
359 design. Cryoegg was deployed in a mesh bag and attached to the main winch (see Figure 4). The
360 receiving antenna was set up in the drill trench, close to the winch (see Fig. 1b). Cryoegg was lowered
361 and raised into the borehole several times and the received signal strength (RSSI) and live data stream
362 monitored at the surface, adjacent to the top of the borehole.



363

364 Figure 4 – Cryoegg ready for deployment on the EastGRIP ice core winch.

365

366 *RESPONDER site at Sermeq Kujalleq*

367 We tested Cryoegg at an inland site (N70° 33.889' W50° 04.558') at Sermeq Kujalleq (Store Glacier),
368 the third fastest outlet glacier in West Greenland (Figure 3). It has a catchment of 35,000 km² that
369 includes supraglacial lakes that periodically drain via cracks and moulins, several on an annual basis
370 (Chudley and others, 2019). The glacier experiences changes in ice flow associated with sudden
371 injections of meltwater to the pressurised drainage system (Doyle and others, 2018), but the link
372 between surface lake drainage and the subglacial hydrology is poorly defined, primarily because
373 instrumenting a draining lake with cabled sensors is near-impossible. There is extensive supporting
374 data available on the subglacial bed structure, lake drainage frequency and ice strain rates (Hofstede
375 and others, 2018; Young and others, 2018; Chudley and others, 2019). Sermeq Kujalleq is the site of
376 the RESPONDER project, offering access to the glacier bed through hot water drilling. The glacier is
377 approximately 1 km thick at this site (Morlighem and others, 2017), and bed access holes were hot
378 water drilled in July 2019.

379 A surface propagation test assessed the range of data transmission through air by monitoring the RSSI
380 and live data stream as the receiving antenna was deployed at a fixed site and Cryoegg hand-carried
381 over a distance of 1.6 km. A hand-held GPS receiver was used to record the position of Cryoegg as it
382 was carried, and the fixed position of the Cryoegg receiver.



384

385 Figure 5 – topographic map of Switzerland showing location of the Rhône Glacier

386

387 The Rhône Glacier is located at N46°34.32' E8°22.58' in the Swiss Alps and is one of the most studied
388 glaciers, with records of front position dating back to the 17th Century (Church and others, 2019). The
389 16 km² glacier is at the pressure melting point throughout and there is an active subglacial drainage
390 network. The glacier is the focus of an intensive subglacial monitoring project, with artificial moulins
391 drilled via hot water in 2018. The moulins remained active in August 2019, when we deployed Cryoegg
392 on the end of a rope tether.

393 Salt dilution gauging (Moore, 2005) was used to estimate moulin discharge. A known quantity of
394 tracer, sodium chloride (NaCl, “table salt”) was added to the supraglacial stream approximately 25 m
395 upstream of the moulin. The discharge can then be calculated from EC readings and the concentration
396 of NaCl added. EC was measured in the supraglacial stream by a Keller DCX-22-CTD 15 m upstream of
397 the moulin and also recorded and transmitted once per second by a Cryoegg lowered into water at
398 the bottom of the moulin.

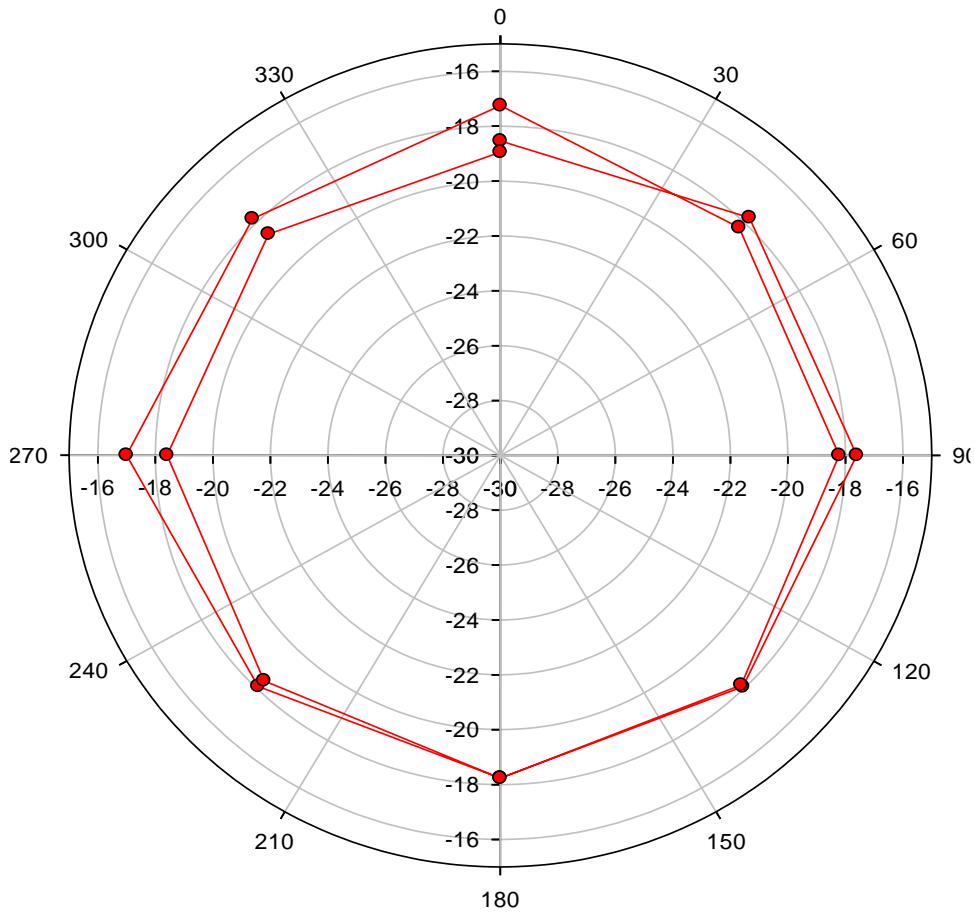
399

400 **RESULTS**

401 **Laboratory RF tests**

402

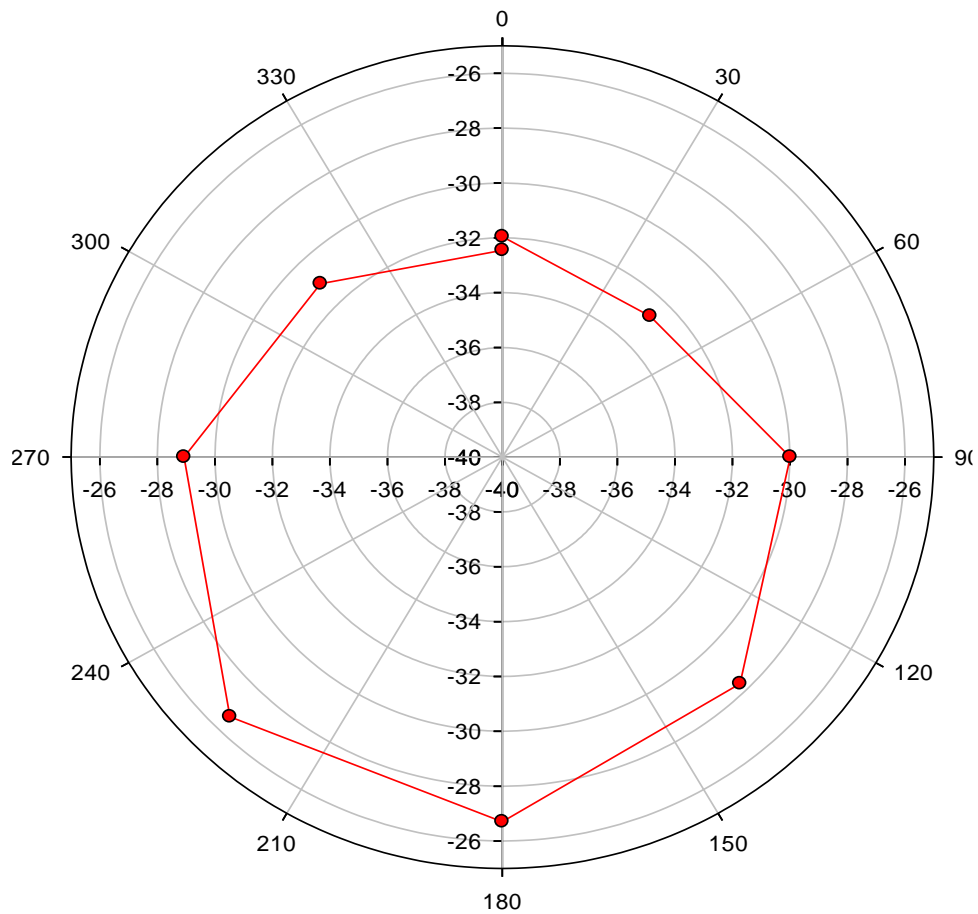
403 RF power meter assessments confirmed that the transmitter put out the full +27 dBm (0.5 W) during
404 each transmission.



405

406 Figure 6 – Horizontal radiation pattern of Cryoegg measured in the RF test chamber

407 The horizontal radiation pattern was measured at eight points around the circumference and is shown
408 in Figure 6. For this measurement the receiving antenna (a log-periodic) was vertically polarised (a
409 brief check showed that this gave a larger signal than when horizontally polarised) and Cryoegg was
410 orientated with its case split line horizontal. Two complete revolutions were measured to check
411 consistency, and it is clear that the pattern is largely omnidirectional, varying by < 2 dB.



412

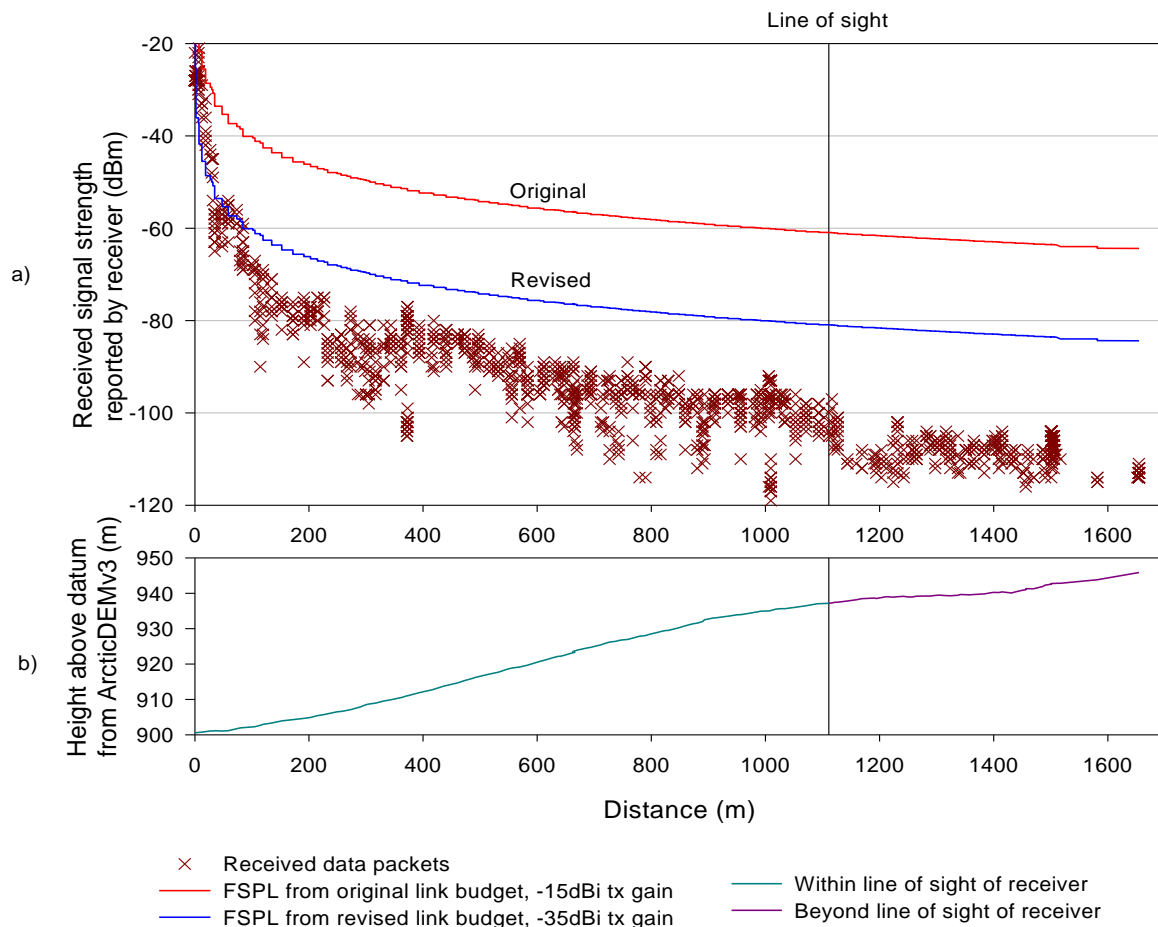
413 Figure 7 – Vertical radiation pattern of Cryoegg measured in the RF test chamber

414 To simulate the RF performance in the borehole, we re-oriented Cryoegg to have the same orientation
 415 as it would have in the borehole, with the split line vertical and normal to the receiving antenna
 416 boresight – i.e. with the crown of the upper half pointing towards the receiving antenna and the
 417 sensor ports pointing away. The receiving antenna was vertically polarised. The results in Figure 7
 418 show that the signal level is significantly lower (10-12 dB) than in the horizontal plane, and that the
 419 pattern is not omnidirectional; there is a 6 dB variation as the unit is rotated.

420

421

422 Surface propagation at Sermeq Kujalleq



423

424 Figure 8 – a) RSSI recorded by receiver during surface range test at Sermeq Kujalleq and expected
 425 received signal strength based on original and revised link budget models (explained in text). b) shows
 426 the ground elevation along the route taken. The black vertical line in both plots shows the point where
 427 the transmitter went beyond the line of sight to the receiver due to the glacier surface topography.

428 Figure 8a shows recorded signal strength for successfully received data packets against range from
 429 the receiver. The terrain profile in Figure 8b was produced from ArcticDEM v3 (Porter and others,
 430 2018) 2 m mosaic values extracted to match the GPS positions recorded in the field. A line of sight
 431 binary was calculated using the QGIS visibility analysis plugin with the receiver height set at 1.5 m and
 432 the transmitter height at 1 m. Given that propagation was mostly in air, and ground reflection on
 433 glaciers is negligible, we expect the signal strength to drop off according to the free space path loss
 434 equation.

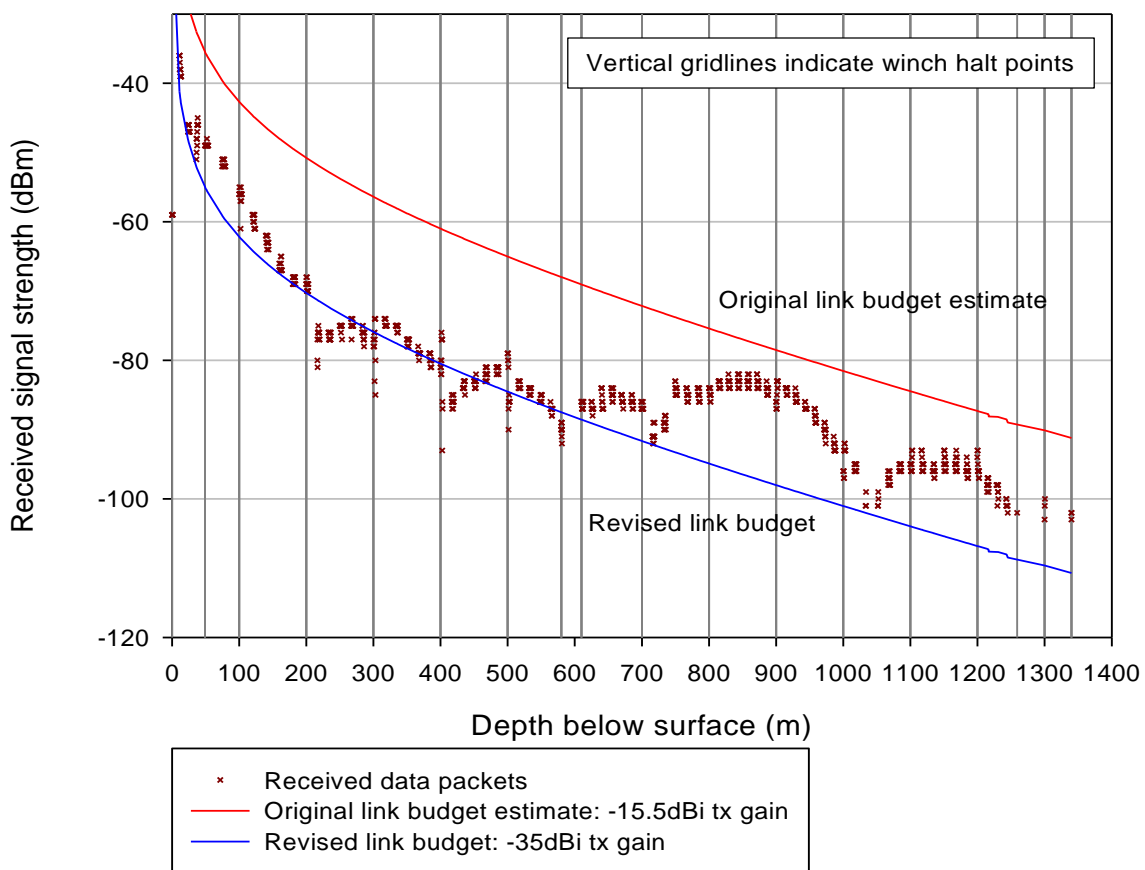
435 Deployment at Sermeq Kujalleq

436 Cryoegg was lowered into a hot water drilled borehole and a moulin. One deployment attempt was
 437 made in the hot water drilled borehole, but the borehole proved too narrow for Cryoegg to pass
 438 through. One data point was obtained with Cryoegg in the borehole about 400 m below the surface,
 439 but it was impossible to proceed further because of borehole refreezing. Moulin deployment was
 440 attempted in a very large moulin (measured at $4.3 \text{ m}^3\text{s}^{-1}$ discharge at the time of deployment) adjacent
 441 to the drill site. Cryoegg was caught in a series of plunge pools and eventually the force of the water
 442 caused it to break free from its tether and it was rapidly swept away out of range. We only obtained
 443 a few data points before losing the signal.

444 **Downhole propagation at EastGRIP**

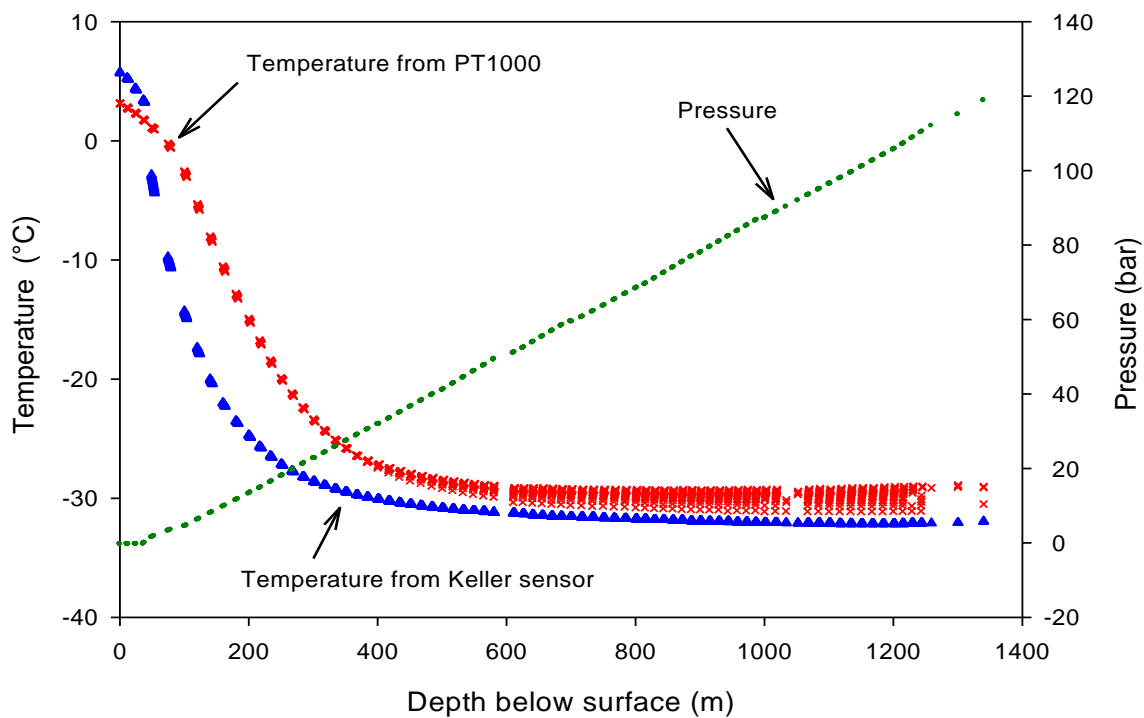
445 At EastGRIP, the borehole is filled with ESTISOL 240 drill fluid rather than water (Sheldon and others,
446 2014). Previous tests at the site (Bagshaw and others, 2018) demonstrated that the fluid had minimal
447 impact on signal propagation. Figure 9 shows the RSSI plotted against depth. Depth is linearly
448 interpolated between depth-measured winch halt points (shown as vertical gridlines on Figure 9),
449 which is a fair assumption because the winch motor speed was constant between these halts. The
450 firmware was configured to produce a burst of 16 packets, one per second, and then wait for 60
451 seconds before the next burst. This accounts for the clustered data points on Figure 9, as all the
452 successfully received packets are plotted.

453 If the transmitted power output from the Cryoegg antenna was constant, and the antenna radiated
454 equally in all directions, and there is no multipath, the plot should be monotonic, with the signal
455 strength always decreasing with depth. However, we can see considerable variations and even
456 retrograde paths, for example between 400 and 500 m; 700-850 m; 1000-1100 m. There are also large
457 variations (>10 dB) in signal level at 300, 400 and 500 m, coinciding with the point where the winch
458 was halted.



459

460 Figure 9 – Received signal strength of successfully-received data packets during a test in the
461 EastGRIP borehole, together with estimated signal strengths produced by link budget calculations.



462

463

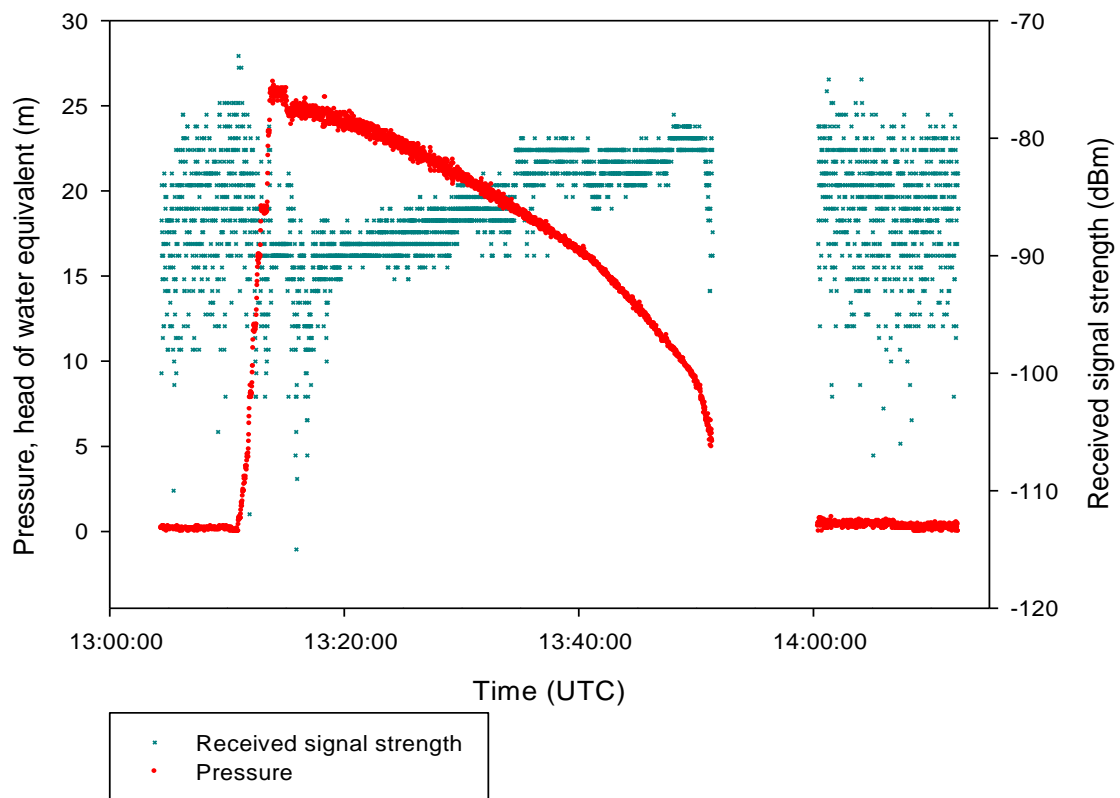
464 Figure 10 – Data received from Cryoegg sensors during the same test in the EastGRIP borehole as
 465 Figure 9.

466 Data from the sensors is shown in Figure 10. The hydrostatic pressure increased with depth – the small
 467 offset is because the drill fluid is around 50 m below the surface level. Data was obtained down to
 468 1340 m, although significant packet loss occurred beyond 1250 m. The two temperature plots
 469 represent data from the two different temperature sensors. The Pt1000 sensor is inside the case,
 470 hence it records a higher temperature for a given depth. The conversion equation from the reported
 471 value (which is in arbitrary units) to temperature is based on theory and has not been confirmed by
 472 calibration. The Keller pressure sensor contains its own temperature sensor, which it uses internally
 473 to compensate the pressure readings against variations in temperature. The high degree of clustering
 474 of the points suggests that the Keller sensor contains some internal averaging, although this may be
 475 caused by the significant mass of the sensor body itself. It is worth noting that Cryoegg was warm
 476 before entering the borehole, so the majority of the temperature data recorded here is simply the
 477 instrument cooling down to the ambient englacial temperature.

478

479 **Moulin drainage at Rhône Glacier**

480 Cryoegg was not able to reach the bed of the Rhône Glacier, 200m below the surface, but instead
481 appeared to be in a deep plunge pool 150m below the surface. Pressure readings received from
482 Cryoegg in real time confirmed that the egg was in up to 25m deep water. Figure 11 shows the
483 pressure recorded whilst Cryoegg was in the plunge pool, and the corresponding received signal
484 strength. There was a sharp rise in pressure as Cryoegg was lowered into the water at 13:12:00 UTC
485 and then a gradual decline over the next 40 minutes. The gap in the data centred on 13:55 was an
486 interruption in the data logging. After the logging resumed, the water pressure had fallen to
487 atmospheric pressure. The reduction in water pressure coincided with a 10dB increase in received
488 signal strength over the same period.



489

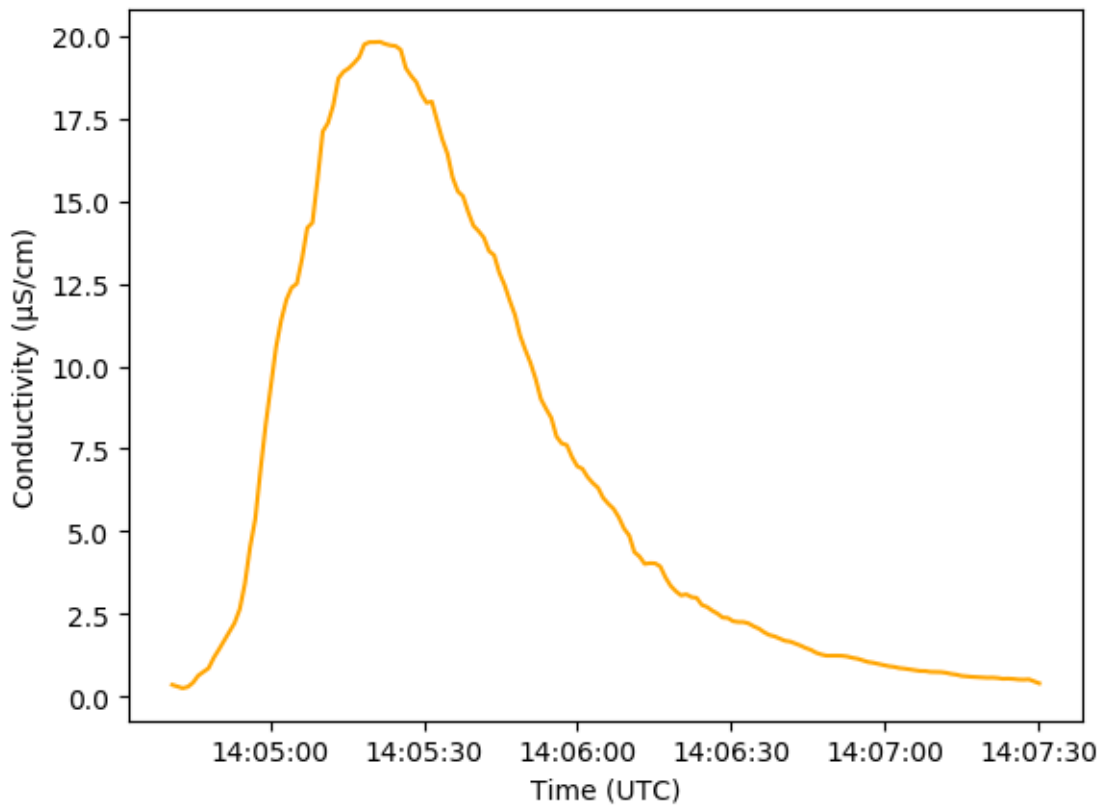
490 Figure 11 – Pressure and received signal strength from Cryoegg when tested in a moulin on Rhône
491 Glacier, 15th August 2019

492

493

494 Salt discharge gauging at Rhône Glacier

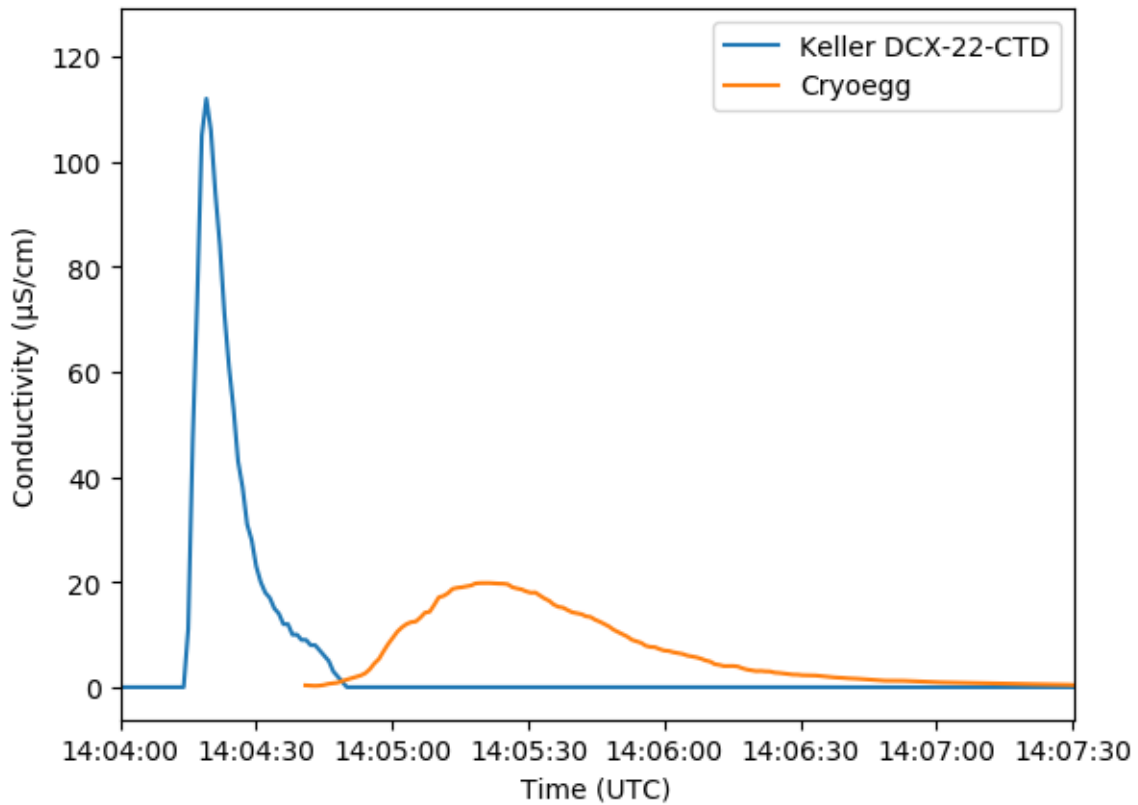
495 Figure 12 shows an example of EC changes as a salt wave passes the Cryoegg, transmitted in real time
496 from the moulin plunge pool at 150 m below the ice surface.



497

498 Figure 12 – reported EC from Cryoegg from within a moulin on Rhône Glacier during a salt slug
499 injection test, 15th August 2019.

500 Simultaneously, the Keller DCX-22-CTD in the supraglacial streams that fed into this same moulin
501 measured the injection of the 100 g l⁻¹ NaCl salt solution 10 m upstream from the logger. Figure 13
502 shows the results from the Keller logger in the stream alongside the results from Cryoegg in the
503 moulin.



504

505 Figure 13 – comparison of salt wave passing Keller logger in the supraglacial stream with Cryoegg
 506 within the moulin. 15th August 2019.

507 The discharge of the supraglacial stream was calculated by the salt dilution as 104 litres s⁻¹ (Moore,
 508 2005), and the discharge within the moulin was slightly higher at 113 litres s⁻¹. The time between the
 509 two peaks was 60 seconds. The velocity of the water between the two instruments was 2.75 m s⁻¹
 510 based on the transit time and the distance between them (15 m in the stream + 150 m down the
 511 moulin = 165 m).

512

513 DISCUSSION

514 Radioglaciological implications

515 The surface range test at Sermeq Kujalleq (Figure 8) indicates that the radiated RF power output of
516 Cryoegg is less than we intended. The upper curve (“Original”) indicates the expected performance
517 for propagation in air if link budget (Table 3) assumptions were correct. In practice the performance
518 is at least 20 dB lower than the original link budget and deteriorates with distance. There are several
519 factors at play here. The main issue appears to be the performance of the transmitting antenna, which
520 is unsurprising since it is electrically very small. We verified experimentally (see “Laboratory RF tests”,
521 above) that the radio module outputs the full +27 dBm, so the lack of output suggests that the antenna
522 is poorly matched to the 50-ohm feed from the radio module, causing power to be wasted. We also
523 verified that the radiation pattern from the antenna is not uniform (Figure 7), which accounts for some
524 of the variations in signal level. Some of the variations in signal level are also terrain-related: it was
525 not practicable to move in a straight line away from the receiving antenna because of crevasses and
526 meltwater streams, so there will be some variation introduced from the radiation pattern of the
527 receiving antenna. Whilst the early part of the test consisted of a gradual ascent up the slope of the
528 glacier, there were numerous ridges and valleys in the surface which had to be climbed over, and
529 these would have resulted in the signal being attenuated by the ice surface. The later part of the test
530 was beyond the line of sight to the receiver (as shown by the elevation profile in Figure 8b), which
531 accounts for the step reduction in signal level beyond 1100 m.

532 We considered the performance in the EastGRIP borehole to be acceptable for a first attempt. We
533 propose a number of candidate explanations as to why no data was received beyond 1340 m depth:

- 534 • Mechanical failure: we know that drill fluid entered the Cryoegg housing during the tests
535 because residues were found inside the housing afterwards. The pressure from the drill fluid
536 is likely to have affected the internal electronics. Of particular concern are the battery (which
537 being a soft “pouch cell” type has no protection from pressure) and connectors, which may
538 be forced apart by non-conductive fluid under high pressure, breaking the circuit.
- 539 • Electrical noise at the receiver prevented weak signals being received
- 540 • Antenna performance: the antennas (transmitting and receiving) provided insufficient gain
- 541 • Ice properties: the attenuation of the ice might be greater than previously thought

542 The receiver gives an indication of received signal strength (RSSI, dBm) for each packet that is
543 successfully received. The receiver data sheet (RC1701xx-MBUS Datasheet, 2018) indicates that the
544 sensitivity (the minimum decodable signal strength) is -119 dBm (1.25 fW), and in other range tests (
545 the surface range test in Figure 8) we succeeded in decoding signals down to this level. However, the
546 RSSI data for the EastGRIP borehole (Figure 9) show that the weakest signals received were only at -
547 103 dBm, 16 dB above the minimum receivable level. Whilst we might have expected a small
548 performance reduction because the site at EastGRIP has electrically noisy machinery, this would not
549 usually account for 16 dB of lost performance. This therefore points more towards a mechanical
550 problem being the primary cause of failure rather than an RF issue, especially given the presence of
551 drill fluid inside the Cryoegg housing at the end of the tests.

552 The output of the original link budget model (Table 3) for the propagation at EastGRIP is shown in
553 Figure 9. This model includes both free-space loss and 21 dB km⁻¹ of ice-related loss. It is clear from
554 both the Sermeq Kujalleq range test (Figure 8) and from the EastGRIP test (Figure 9) that the radiated
555 output from Cryoegg was at least 20 dB lower than was allowed for in the original link budget.
556 Replotting the link budget using the same value (21 dB km⁻¹) for the ice attenuation coefficient but
557 adjusting the transmit power down by 20dB produced the “revised link budget” curve plotted on

558 Figure 8 and Figure 9. This fits closely to the data up to around 600 m, where ice-related attenuation
559 is still a relatively small factor, suggesting that the transmit power estimate is broadly correct. Beyond
560 600 m the revised link budget becomes a conservative estimate for the performance in deep ice. It is
561 highly likely that the attenuation coefficient is not constant throughout the borehole, but for our
562 purposes we require a realistic but conservative estimate for the ice attenuation in order to be sure
563 of the link performance in future iterations of the Cryoegg design. The first 90 m of the borehole is
564 surrounded by firn (Vallelonga and others, 2014, (Fig. 9)), whereas the lower section is in glacier ice,
565 and the changes of material properties both from firn to ice and within the ice itself will cause some
566 variation in attenuation coefficient (Bagshaw and others 2018). These variations notwithstanding, this
567 data confirms that 21 dB km^{-1} (see section “Choice of frequency / radio propagation in ice” above) was
568 a safe choice for the ice attenuation coefficient in our link budget.

569 The large (>10 dB) variation in signal strength observed at several winch halt points is most likely
570 caused by Cryoegg rotating on the vertical axis as the wire rope twists. The deceleration of the winch
571 will result in some of the momentum of Cryoegg and the cable being converted into torsional forces
572 on the winch cable, with Cryoegg twisting back and forth on the end of the cable. This then indicates
573 that the antenna radiation pattern is not as uniform as we had hoped and is perhaps also being
574 adversely influenced by the presence of the metal winch cable. The non-uniformity of the radiation
575 pattern is confirmed by our laboratory tests (Figure 7).

576 The signal strength plot (Figure 9) appears to show a number of nulls – locations where the signal
577 strength drops significantly – notably at around 600 m and 1040 m. Nulls are often produced by
578 multipath effects, where the signal reflected off a surface interferes destructively with the direct signal
579 at the receiver (Griffiths, 1987, 102–104). However, in this case there is no obvious candidate for the
580 reflecting surface: the geometry required to produce widely-spaced large nulls rules out horizontal
581 reflectors like the glacier bed or internal layers. The shear margin is too far away (5 km) to produce
582 this type of null. More data will be required to determine whether these nulls are equipment related
583 or caused by some property of the ice stream’s structure.

584 The performance of the radio link in the Rhône glacier moulin (Figure 11) was also satisfactory. We
585 anticipated that the temperate ice and presence of flowing water would increase the overall
586 attenuation. Figure 11 shows that the signal propagating through 25 m of meltwater and a further 125
587 m of temperate ice to the glacier surface was attenuated to -90 dBm. This compares with the EastGRIP
588 borehole (Figure 9) where this signal strength was reached after more than 500 m. The reduction in
589 observed moulin water pressure, indicative of 25m head of water draining out of the moulin, produced
590 an increase in RSSI by around 10 dB. This confirms that the presence of liquid water increases the
591 signal attenuation.

592 The variation in signal is much greater when Cryoegg is in the “atmospheric pressure” region of the
593 moulin rather than when it is in >1 m of water (Figure 11). When Cryoegg is reporting pressure close
594 to atmospheric pressure, it is being splashed by the water, or water is flowing smoothly past it. In this
595 scenario the water flow will spin and agitate Cryoegg on the end of the rope, creating variation in
596 signal level because of the antenna pattern. The turbulent flow of the water will also create ever-
597 changing levels of attenuation. However, once Cryoegg is below the water surface, the viscosity of the
598 water will reduce its spinning and agitation, and the attenuation due to the water will be constant.

599

600 **Glaciohydrological implications**

601 The water pressure recorded by Cryoegg in the moulin steadily decreased during the 40 minutes that
602 it remained in the plunge pool (Figure 11). Eventually, the water level dropped below Cryoegg and it
603 returned to atmospheric pressure with the characteristic fluctuations in RSSI caused by splashing
604 water. We interpret this as dynamic drainage of the plunge pool over the afternoon, as water backed
605 up in the drainage system forces its way to the glacier bed. Similar pressure variations have been
606 previously observed in moulins (Iken, 1972; Röthlisberger, 1980; Holmlund and Hooke, 1983) and
607 demonstrate that the subglacial drainage system is not in equilibrium but constantly fluctuating
608 (Röthlisberger and Lang, 1987). The characteristic step-pool system develops if the moulin persists for
609 more than one season (Gulley, 2009); the artificial moulin was drilled directly to the end in 2018, but
610 by 2019 was 'kinked' and a plunge pool formed approximately 50 m above the bed.

611 Simultaneous salt tracing in a supraglacial stream feeding the moulin and within the moulin itself
612 shows (Figure 13) that the moulin discharge was slightly higher than the stream discharge –
613 unsurprising, as the stream that we measured was not the sole supply of water feeding the moulin.
614 This experiment demonstrates Cryoegg's potential for measuring hydrological parameters in locations
615 that are difficult to access. Previously, moulin discharge has been estimated at the surface (either by
616 field measurements or remote sensing), which masks the effect of water being stored within the
617 vertical column of the moulin itself (Werder and others, 2010). We show that it is possible to monitor
618 supraglacial discharge, the height of the stored water column within the moulin, and the moulin
619 discharge simultaneously and in real time, providing a valuable new approach for future studies of
620 glacier hydrology.

621 **Comparison with other wireless subglacial probes**

622 The most successful wireless subglacial probe for deep ice has been the WiSe system (Smeets and
623 others, 2012). This was demonstrated returning a signal through 2500 m of ice in Greenland. This
624 system operated at 30 MHz in order to benefit from lower free-space attenuation, but at the expense
625 of making the antennas very large. The WiSe system suffered from some skywave interference
626 affecting signal reception, which is a particular issue at 30 MHz and below, and required use of a large
627 (5 m long) HB9CV type antenna to mitigate against it. WiSe required a 1 W (+30 dBm) transmitter to
628 communicate at depths of more than 2000 m, but it is not clear not how much of this power was
629 actually radiated – the ferrite-loaded antenna used was likely to be very lossy.

630 Our probe and receiving antenna are both more compact than the WiSe system and we use
631 commercially-available radio modules that adhere to an international open standard, which means
632 that the key components are likely to be readily available well into the future.

633 The GlacsWeb system originally operated at 433 MHz (Martinez and others, 2004) but later (Martinez
634 and others, 2013) used 151 MHz, giving a maximum reported range in ice of 70 m (Hart and others,
635 2019). Cryoegg is specifically designed for deep ice, and hence our radio performance greatly exceeds
636 that of GlacsWeb, enabling its use in at least 1000 m of ice.

637 **CONCLUSION AND OUTLOOK**

638 We have undertaken a full re-design of the wireless subglacial sensor platform Cryoegg, using a new
639 radio link technology and improved link budget design, and demonstrate that it can transmit sensor
640 data in real time through more than 1.3 km of cold ice. Deployments in moulins in temperate ice show
641 that Cryoegg is a valuable tool for recording englacial and subglacial hydrological properties in situ,
642 and hence giving further insight into processes in these environments. The EC sensor, originally
643 intended as a proxy for total dissolved solids in subglacial water, can facilitate salt dilution gauging for

644 estimates of discharge. Real-time data transmission made for efficient fieldwork, allowing immediate
645 confirmation of equipment operation and information about the target environment. All sensors
646 operated well, revealing englacial conditions and demonstrating their applicability for future
647 subglacial deployments. The sensors fitted to the existing design were chosen because of their ease
648 of implementation and their applicability to studies of subglacial hydrology, but Cryoegg can be
649 adapted to support other sensors.

650 Future developments will refine and enhance the design, particularly with respect to the antenna
651 performance and mechanical design, so that we have a robust instrument capable of returning data
652 for months or years through 2.5 km of ice. This would enable us to match the performance of the WiSe
653 system (Smeets and others, 2012) but with more compact antennas, enabling the Cryoegg to ‘roam’
654 through englacial and subglacial hydrological systems to collect spatially and temporally distributed
655 measurements, reported in real time. Cryoegg technology will also be adapted for englacial studies
656 in irregular and refreezing hot-water-drilled boreholes, by creating a cylindrical form factor with a
657 much smaller diameter than Cryoegg, allowing deployment in a smaller borehole.

658 **ACKNOWLEDGEMENTS**

659 This work was funded by UK Engineering and Physical Sciences Research Council (EPSRC) New
660 Investigator Award EP/R03530X/1.

661 Thanks to all who assisted us in the field, in particular: Trevor Popp, Romain Duphil and the EastGRIP
662 drill team; “Mickey” MacKay, Eliza Dawson and Rob Law at the RESPONDER site; Lai Bun Lok, Jonathan
663 Hawkins, the ETH Zürich VAW Glaciology team and the Swiss Air Force at the Rhône Glacier site. Phil
664 Anderson gave us use of the RF test chamber. We are grateful for in-kind contributions of equipment
665 from Quadro and Radiocrafts. Particular thanks to the team at DGF Engineering for the machining of
666 the caseworks, and to Protronix EMS Ltd for the rapid production of the electronics. Miles Gould
667 provided assistance with the algebra for Equation 3.

668 EastGRIP is directed and organized by the Center of Ice and Climate at the Niels Bohr Institute. It is
669 supported by funding agencies and institutions in Denmark (A. P. Møller Foundation, University of
670 Copenhagen), USA (US National Science Foundation, Office of Polar Programs), Germany (Alfred
671 Wegener Institute, Helmholtz Centre for Polar and Marine Research), Japan (National Institute of Polar
672 Research and Arctic Challenge for Sustainability), Norway (University of Bergen and Bergen Research
673 Foundation), Switzerland (Swiss National Science Foundation), France (French Polar Institute Paul-
674 Emile Victor, Institute for Geosciences and Environmental research) and China (Chinese Academy of
675 Sciences and Beijing Normal University)

676 Bryn Hubbard acknowledges support for hot-water borehole drilling from HEFCW through a Capital
677 Equipment Grant awarded to Aberystwyth University, and from the NERC through grant NE/K006126.

678 The RESPONDER project is funded by a Consolidator Grant to Poul Christoffersen from the European
679 Research Council, under the European Union’s Horizon 2020 research and innovation programme.

680 Tom Chudley was supported by a Natural Environment Research Council Doctoral Training Partnership
681 Studentship (Grant NE/L002507/1).

682 ArcticDEM was created from DigitalGlobe, Inc., imagery and funded under National Science
683 Foundation awards 1043681, 1559691, and 1542736

684

685 SUPPLEMENTARY MATERIAL

686

Activity	Quantity	Unit
Energy consumption during measure and transmit	0.5	J
Duration of measure and transmit	3.2	s
Current consumption during sleep	500	nA
Nominal battery voltage	3.7	V
Power consumption during sleep	1.85	uW
Battery nominal voltage	3.7	V
Battery nominal capacity	400	mAh
Battery nominal capacity	1.48	Wh
Battery nominal capacity	5328	J
Derate factor for operating in the cold	50%	
Battery effective capacity in the field	2664	J
For 2 measurements per day:		
Active measurement time per day:	6.4	seconds
Sleep time per day	86393.6	seconds
Energy used whilst active	1	J
Energy used whilst asleep	0.16	J
Total energy used per day	1.16	J
Number of days the system will run for	2296	days
Number of years the system will run for	6.3	years

687 Table S1 – battery life calculation

688

689

690

691 REFERENCES

692

693 About LoRaWAN® | LoRa Alliance® <https://lora-alliance.org/about-lorawan>

694 Bagshaw EA, Burrow S, Wadham JL, Bowden J, Lishman B, Salter M, Barnes R and
695 Nienow P (2012) E-tracers: Development of a low cost wireless technique for
696 exploring sub-surface hydrological systems. *Hydrological Processes* **26**(20), 3157–
697 3160 (doi:10.1002/hyp.9451)

698 Bagshaw E, Karlsson NB, Lishman B, Lok LB, Burrow S, Wadham JL, Clare L, Nicholls
699 KW, Eisen O, Corr HFJ and Dahl-Jensen D (2018) Utilising Wireless Sensor
700 Technologies in Glaciology. *AGU Fall Meeting Abstracts* **43**
701 <http://adsabs.harvard.edu/abs/2018AGUFM.C43D1823B>

702 Bagshaw EA, Lishman B, Wadham JL, Bowden JA, Burrow SG, Clare LR and Chandler D
703 (2014) Novel wireless sensors for in situ measurement of sub-ice hydrologic systems.
704 *Annals of Glaciology* **55**(65), 41–50 (doi:10.3189/2014AoG65A007)

705 Barrella T, Barwick S and Saltzberg D (2011) Ross Ice Shelf in situ radio-frequency ice
706 attenuation. *Journal of Glaciology* **57**(201), 61–66
707 (doi:10.3189/002214311795306691)

708 Barwick S, Besson D, Gorham P and Saltzberg D (2005) South Polar in situ radio-frequency
709 ice attenuation. *Journal of Glaciology* **51**(173), 231–238
710 (doi:10.3189/172756505781829467)

711 Broeke MR van den, Enderlin EM, Howat IM, Kuipers Munneke P, Noël BPY, Berg WJ van
712 de, Meijgaard E van and Wouters B (2016) On the recent contribution of the
713 Greenland ice sheet to sea level change. *The Cryosphere* **10**(5), 1933–1946
714 (doi:<https://doi.org/10.5194/tc-10-1933-2016>)

715 Chandler DM, Wadham JL, Lis GP, Cowton T, Sole A, Bartholomew I, Telling J, Nienow P,
716 Bagshaw EB, Mair D, Vinen S and Hubbard A (2013) Evolution of the subglacial
717 drainage system beneath the Greenland Ice Sheet revealed by tracers. *Nature Geosci*
718 **6**(3), 195–198 (doi:10.1038/ngeo1737)

719 Chu VW (2014) Greenland ice sheet hydrology: A review. *Progress in Physical Geography:*
720 *Earth and Environment* **38**(1), 19–54 (doi:10.1177/0309133313507075)

721 Chudley TR, Christoffersen P, Doyle SH, Bougamont M, Schoonman CM, Hubbard B and
722 James MR (2019) Supraglacial lake drainage at a fast-flowing Greenlandic outlet
723 glacier. *PNAS* **116**(51), 25468–25477 (doi:10.1073/pnas.1913685116)

724 Church G, Bauder A, Grab M, Rabenstein L, Singh S and Maurer H (2019) Detecting and
725 characterising an englacial conduit network within a temperate Swiss glacier using
726 active seismic, ground penetrating radar and borehole analysis. *Annals of Glaciology*
727 **60**(79), 193–205 (doi:10.1017/aog.2019.19)

- 728 Clarke GKC (1987) Subglacial till: A physical framework for its properties and processes.
 729 *Journal of Geophysical Research: Solid Earth* **92**(B9), 9023–9036
 730 (doi:10.1029/JB092iB09p09023)
- 731 Doyle SH, Hubbard B, Christoffersen P, Young TJ, Hofstede C, Bougamont M, Box JE and
 732 Hubbard A (2018) Physical Conditions of Fast Glacier Flow: 1. Measurements From
 733 Boreholes Drilled to the Bed of Store Glacier, West Greenland. *Journal of*
 734 *Geophysical Research: Earth Surface* **123**(2), 324–348 (doi:10.1002/2017JF004529)
- 735 European Committee for Standardisation (2013) *BS EN 13757-4:2013 - Communication*
 736 *systems for meters and remote reading of meters . Wireless meter readout (Radio*
 737 *meter reading for operation in SRD bands)*. [https://bsol.bsigroup.com/en/Bsol-Item-](https://bsol.bsigroup.com/en/Bsol-Item-Detail-Page/?pid=000000000030249978)
 738 [Detail-Page/?pid=000000000030249978](https://bsol.bsigroup.com/en/Bsol-Item-Detail-Page/?pid=000000000030249978)
- 739 Flowers GE (2018) Hydrology and the future of the Greenland Ice Sheet. *Nature*
 740 *Communications* **9**(1), 2729 (doi:10.1038/s41467-018-05002-0)
- 741 Friis HT (1946) A Note on a Simple Transmission Formula. *Proceedings of the IRE* **34**(5),
 742 254–256 (doi:10.1109/JRPROC.1946.234568)
- 743 Griffiths J (1987) *Radio wave propagation and antennas*. Prentice-Hall
- 744 Gulley J (2009) Structural control of englacial conduits in the temperate Matanuska Glacier,
 745 Alaska, USA. *Journal of Glaciology* **55**(192), 681–690
 746 (doi:10.3189/002214309789470860)
- 747 Hart JK, Martinez K, Basford PJ, Clayton AI, Robson BA and Young DS (2019) Surface
 748 melt driven summer diurnal and winter multi-day stick-slip motion and till
 749 sedimentology. *Nat Commun* **10**(1), 1–11 (doi:10.1038/s41467-019-09547-6)
- 750 Hoffman MJ, Andrews LC, Price SF, Catania GA, Neumann TA, Lüthi MP, Gulley J, Ryser
 751 C, Hawley RL and Morriss B (2016) Greenland subglacial drainage evolution
 752 regulated by weakly connected regions of the bed. *Nat Commun* **7**(1), 1–12
 753 (doi:10.1038/ncomms13903)
- 754 Hofstede C, Christoffersen P, Hubbard B, Doyle SH, Young TJ, Diez A, Eisen O and
 755 Hubbard A (2018) Physical Conditions of Fast Glacier Flow: 2. Variable Extent of
 756 Anisotropic Ice and Soft Basal Sediment From Seismic Reflection Data Acquired on
 757 Store Glacier, West Greenland. *Journal of Geophysical Research: Earth Surface*
 758 **123**(2), 349–362 (doi:10.1002/2017JF004297)
- 759 Holmlund P and Hooke RLeb (1983) High Water-Pressure Events in Moulins, Storglaciären,
 760 Sweden. *Geografiska Annaler: Series A, Physical Geography* **65**(1–2), 19–25
 761 (doi:10.1080/04353676.1983.11880070)
- 762 Hubbard BP, Sharp MJ, Willis IC, Nielsen MK and Smart CC (1995) Borehole water-level
 763 variations and the structure of the subglacial hydrological system of Haut Glacier
 764 d’Arolla, Valais, Switzerland. *Journal of Glaciology* **41**(139), 572–583
 765 (doi:10.3189/S0022143000034894)

- 766 Iken A (1972) Measurements of Water Pressure in Moulins as Part of a Movement Study of
767 the White Glacier, Axel Heiberg Island, Northwest Territories, Canada. *Journal of*
768 *Glaciology* **11**(61), 53–58 (doi:10.3189/S0022143000022486)
- 769 Iken A (1981) The Effect of the Subglacial Water Pressure on the Sliding Velocity of a
770 Glacier in an Idealized Numerical Model. *Journal of Glaciology* **27**(97), 407–421
771 (doi:10.3189/S0022143000011448)
- 772 Iken A and Bindshadler RA (1986) Combined measurements of Subglacial Water Pressure
773 and Surface Velocity of Findelengletscher, Switzerland: Conclusions about Drainage
774 System and Sliding Mechanism. *Journal of Glaciology* **32**(110), 101–119
775 (doi:10.3189/S0022143000006936)
- 776 Iken A, Echelmeyer K, Harrison W and Funk M (1993) Mechanisms of fast flow in
777 Jakobshavns Isbræ, West Greenland: Part I. Measurements of temperature and water
778 level in deep boreholes. *Journal of Glaciology* **39**(131), 15–25
779 (doi:10.3189/S0022143000015689)
- 780 Joughin I (2017) MEaSURES Greenland Ice Velocity Annual Mosaics from SAR and
781 Landsat, Version 1. (doi:10.5067/OBXCG75U7540)
- 782 Joughin I, Smith BE, Howat IM, Scambos T and Moon T (2010) Greenland flow variability
783 from ice-sheet-wide velocity mapping. *Journal of Glaciology* **56**(197), 415–430
784 (doi:10.3189/002214310792447734)
- 785 Kamb B (1970) Sliding motion of glaciers: Theory and observation. *Reviews of Geophysics*
786 **8**(4), 673–728 (doi:10.1029/RG008i004p00673)
- 787 Kamb B (1987) Glacier surge mechanism based on linked cavity configuration of the basal
788 water conduit system. *Journal of Geophysical Research: Solid Earth* **92**(B9), 9083–
789 9100 (doi:10.1029/JB092iB09p09083)
- 790 Karlsson NB and Dahl-Jensen D (2015) Response of the large-scale subglacial drainage
791 system of Northeast Greenland to surface elevation changes. *The Cryosphere* **9**(4),
792 1465–1479 (doi:https://doi.org/10.5194/tc-9-1465-2015)
- 793 Lewis C, Gogineni S, Rodriguez-Morales F, Panzer B, Stumpf T, Paden J and Leuschen C
794 (2015) Airborne fine-resolution UHF radar: an approach to the study of englacial
795 reflections, firn compaction and ice attenuation rates. *J. Glaciol.* **61**(225), 89–100
796 (doi:10.3189/2015JoG14J089)
- 797 Martinez K, Basford PJ, Jager DD and Hart JK (2013) Using a heterogeneous sensor network
798 to monitor glacial movement. 2
- 799 Martinez K, Ong R and Hart J (2004) Glacsweb: a sensor network for hostile environments.
800 *2004 First Annual IEEE Communications Society Conference on Sensor and Ad Hoc*
801 *Communications and Networks, 2004. IEEE SECON 2004.* 81–87
802 (doi:10.1109/SAHCN.2004.1381905)
- 803 Moore RD (2005) Introduction to salt dilution gauging for streamflow measurement Part 3:
804 Slug injection using salt in solution. *Streamline Watershed Management Bulletin* **8**(2),
805 1–6

- 806 Morlighem M, Williams CN, Rignot E, An L, Arndt JE, Bamber JL, Catania G, Chauché N,
807 Dowdeswell JA, Dorschel B, Fenty I, Hogan K, Howat I, Hubbard A, Jakobsson M,
808 Jordan TM, Kjeldsen KK, Millan R, Mayer L, Mouginot J, Noël BPY, O’Cofaigh C,
809 Palmer S, Rysgaard S, Seroussi H, Siegert MJ, Slabon P, Straneo F, van den Broeke
810 MR, Weinrebe W, Wood M and Zinglensen KB (2017) BedMachine v3: Complete
811 Bed Topography and Ocean Bathymetry Mapping of Greenland From Multibeam
812 Echo Sounding Combined With Mass Conservation. *Geophysical Research Letters*
813 **44**(21), 11,051–11,061 (doi:10.1002/2017GL074954)
- 814 Ng FSL (2000) Canals under sediment-based ice sheets. *Annals of Glaciology* **30**, 146–152
815 (doi:10.3189/172756400781820633)
- 816 Nienow PW, Hubbard AL, Hubbard BP, Chandler DM, Mair DWF, Sharp MJ and Willis IC
817 (2005) Hydrological controls on diurnal ice flow variability in valley glaciers. *Journal*
818 *of Geophysical Research: Earth Surface* **110**(F4) (doi:10.1029/2003JF000112)
- 819 Nienow PW, Sole AJ, Slater DA and Cowton TR (2017) Recent Advances in Our
820 Understanding of the Role of Meltwater in the Greenland Ice Sheet System. *Curr*
821 *Clim Change Rep* **3**(4), 330–344 (doi:10.1007/s40641-017-0083-9)
- 822 Nye JF (1976) Water Flow in Glaciers: Jökulhlaups, Tunnels and Veins. *Journal of*
823 *Glaciology* **17**(76), 181–207 (doi:10.3189/S002214300001354X)
- 824 Plewes LA and Hubbard B (2016) A review of the use of radio-echo sounding in glaciology:
825 *Progress in Physical Geography* (doi:10.1177/030913330102500203)
- 826 Porter C, Morin P, Howat I, Noh M-J, Bates B, Peterman K, Keesey S, Schlenk M, Gardiner
827 J, Tomko K, Willis M, Kelleher C, Cloutier M, Husby E, Foga S, Nakamura H,
828 Platson M, Wethington M Jr, Williamson C, Bauer G, Enos J, Arnold G, Kramer W,
829 Becker P, Doshi A, D’Souza C, Cummens P, Laurier F and Bojesen M (2018)
830 ArcticDEM. (doi:10.7910/DVN/OHHUKH)
- 831 Pritchard HD, Arthern RJ, Vaughan DG and Edwards LA (2009) Extensive dynamic thinning
832 on the margins of the Greenland and Antarctic ice sheets. *Nature* **461**(7266), 971–975
833 (doi:10.1038/nature08471)
- 834 RC1701xx-MBUS Datasheet (2018) [https://radiocrafts.com/uploads/rc1701xx-
mbus_datasheet.pdf](https://radiocrafts.com/uploads/rc1701xx-
835 mbus_datasheet.pdf)
- 836 Röthlisberger H (1972) Water Pressure in Intra- and Subglacial Channels *. *Journal of*
837 *Glaciology* **11**(62), 177–203 (doi:10.3189/S0022143000022188)
- 838 Röthlisberger H (1980) Gletscherbewegung und Wasserabfluss. *Wasser, Energie, Luft* **72**(9),
839 290–294
- 840 Röthlisberger H and Lang H (1987) Glacial Hydrology. *Glacio-Fluvial Sediment Transfer:*
841 *An Alpine Perspective*. Wiley, 207–84
- 842 Schoof C (2010) Ice-sheet acceleration driven by melt supply variability. *Nature* **468**(7325),
843 803–806 (doi:10.1038/nature09618)

- 844 Sheldon SG, Steffensen JP, Hansen SB, Popp TJ and Johnsen SJ (2014) The investigation
845 and experience of using ESTISOL™ 240 and COASOL™ for ice-core drilling.
846 *Annals of Glaciology* **55**(68), 219–232 (doi:10.3189/2014AoG68A036)
- 847 Smeets CJPP, Boot W, Hubbard A, Pettersson R, Wilhelms F, Broeke MRVD and Wal
848 RSWVD (2012) A wireless subglacial probe for deep ice applications. *Journal of*
849 *Glaciology* **58**(211), 841–848 (doi:10.3189/2012JoG11J130)
- 850 Sole AJ, Mair DWF, Nienow PW, Bartholomew ID, King MA, Burke MJ and Joughin I
851 (2011) Seasonal speedup of a Greenland marine-terminating outlet glacier forced by
852 surface melt-induced changes in subglacial hydrology. *Journal of Geophysical*
853 *Research: Earth Surface* **116**(F3) (doi:10.1029/2010JF001948)
- 854 Tedstone AJ, Nienow PW, Gourmelen N, Dehecq A, Goldberg D and Hanna E (2015)
855 Decadal slowdown of a land-terminating sector of the Greenland Ice Sheet despite
856 warming. *Nature* **526**(7575), 692–695 (doi:10.1038/nature15722)
- 857 Tranter M, Sharp MJ, Lamb HR, Brown GH, Hubbard BP and Willis IC (2002) Geochemical
858 weathering at the bed of Haut Glacier d’Arolla, Switzerland—a new model.
859 *Hydrological Processes* **16**(5), 959–993 (doi:10.1002/hyp.309)
- 860 UM10204 I2C-bus specification and user manual (2014) **2014**, 64
- 861 Vallelonga P, Christianson K, Alley RB, Anandakrishnan S, Christian JEM, Dahl-Jensen D,
862 Gkinis V, Holme C, Jacobel RW, Karlsson NB, Keisling BA, Kipfstuhl S, Kjær HA,
863 Kristensen MEL, Muto A, Peters LE, Popp T, Riverman KL, Svensson AM, Tibuleac
864 C, Vinther BM, Weng Y and Winstrup M (2014) Initial results from geophysical
865 surveys and shallow coring of the Northeast Greenland Ice Stream (NEGIS). *The*
866 *Cryosphere* **8**(4), 1275–1287 (doi:10.5194/tc-8-1275-2014)
- 867 Walder JS (1986) Hydraulics of Subglacial Cavities. *Journal of Glaciology* **32**(112), 439–445
868 (doi:10.3189/S0022143000012156)
- 869 Werder MA, Schuler TV and Funk M (2010) Short term variations of tracer transit speed on
870 alpine glaciers. *The Cryosphere* **4**(3), 381–396 (doi:https://doi.org/10.5194/tc-4-381-
871 2010)
- 872 Young TJ, Schroeder DM, Christoffersen P, Lok LB, Nicholls KW, Brennan PV, Doyle SH,
873 Hubbard B and Hubbard A (2018) Resolving the internal and basal geometry of ice
874 masses using imaging phase-sensitive radar. *Journal of Glaciology* **64**(246), 649–660
875 (doi:10.1017/jog.2018.54)
- 876
- 877